Draft version June 26, 2014
Preprint typeset using LaTeX style emulateapj v. 5/2/11

THE CRITERION OF SUPERNOVA EXPLOSION REVISITED: THE MASS ACCRETION HISTORY

Yudai Suwa[1,2], Shoichi Yamada[3,4], Tomoya Takiwaki[5], and Kei Kotake[6,5]

Draft version June 26, 2014

ABSTRACT

By performing neutrino-radiation hydrodynamic simulations in spherical symmetry (1D) and axial symmetry (2D) with different progenitor models by Woosley & Heger (2007) from 12 $M_\odot$ to 100 $M_\odot$, we find that all 1D runs fail to produce explosion and several 2D runs succeed. The difference of shock evolution can be interpreted by the difference of mass accretion history, which is determined by the density structure of the progenitor. The exploding models exhibit high neutrino luminosity with low mass accretion rate. This is consistent with the discussion about the so-called critical curve in the mass accretion rate and neutrino luminosity plane, above which there is no steady solution of the accretion flow so that a dynamical expanding shock wave is expected. In addition, we developed a phenomenological model to evaluate the trajectories in this plane. This model reasonably reproduces the numerical results by using the initial density structure of the progenitors alone. By this model, we can predict the possibility of explosion by using the initial density structure of the progenitors alone.

Subject headings: supernovae: general — hydrodynamics — neutrinos

1. INTRODUCTION

Core-collapse supernova is one of the most energetic explosions in the universe. Although the explosion mechanism is still under a thick veil, there are a few candidates. Among them, neutrino heating mechanism is the most promising scenario, in which a copious amount of neutrinos are emitted in the vicinity of protoneutron star (PNS) and are partially absorbed by the postshock material. In this system, neutrinos transfer the internal energy from inside to outside and act effectively as a heating source for the postshock layer.

Although this neutrino-heating mechanism firmly works, state-of-the-art simulations of neutrino-radiation hydrodynamics can not produce explosion in spherical symmetry (Rampp & Janka 2000; Liebendörfer et al. 2001; Thompson et al. 2003; Sumiyoshi et al. 2005). Recently, modern multi-dimensional simulations became possible and several exploding simulations have been reported (Buras et al. 2006; Marek & Janka 2009; Suwa et al. 2010; Müller et al. 2012b; Bruenn et al. 2013 in two dimensions (2D) and Takiwaki et al. 2012; Hanke et al. 2013 in three dimensions (3D)). These simulations basically focused on limited progenitors such as[7]

- 11.2 $M_\odot$ of Woosley et al. (2002): Buras et al. (2006); Marek & Janka (2009); Takiwaki et al. (2012); Müller et al. (2012b); Suwa et al. (2013); Suwa (2014); Takiwaki et al. (2014)
- 13 $M_\odot$ of Nomoto & Hashimoto (1988): Suwa et al. (2010, 2011)
- 15 $M_\odot$ of Woosley & Weaver (1995): Buras et al. (2006); Marek & Janka (2009); Suwa et al. (2011); Müller et al. (2012b); Suwa et al. (2013)
- 27 $M_\odot$ of Woosley et al. (2002): Müller et al. (2012a); Hanke et al. (2013)

Recently, Bruenn et al. (2013) performed a systematic study using a progenitor series of Woosley & Heger (2007) from 12 $M_\odot$ to 25 $M_\odot$ and found similar explosions for all progenitors. However, Dolence et al. (2014) reported that they found none of them results in explosion. In this study, we perform two-dimensional simulations of a broader mass range from 12 $M_\odot$ to 100 $M_\odot$ using the same progenitor series (Woosley & Heger 2007).

The progenitor structure is one of the most important ingredients of core-collapse supernova explosion mechanism[8] because it determines the initial condition and later accretion rate history. The mass accretion rate is strongly related to the shock wave evolution since the force balance between the ram pressure of preshocked material and the thermal pressure of postshocked material determines the shock position. The mass accretion rate, $\dot{M} = 4\pi r^2 \rho v$, can be a good measure of the ram pressure, ρv^2. Indeed, an O-Ne-Mg core with an 8.8 $M_\odot$ star can easily produce an explosion even in spherical symmetry thanks to rapid decrease of the mass accretion rate onto the shock (Kitaura et al. 2006).

Recently, the progenitor dependence of the supernova dynamics is attracting great attention. Ugliano et al.

[1] Yukawa Institute for Theoretical Physics, Kyoto University, Oiwake-cho, Kitashirakawa, Sakyo-ku, Kyoto, 606-8502, Japan
[2] Max-Planck-Institut für Astrophysik, Karl-Schwarzschild-Str. 1, D-85748 Garching, Germany
[3] Department of Physics, Waseda University, 3-4-1 Okubo, Shinjuku, Tokyo 169-8555, Japan
[4] Advanced Research Institute for Science & Engineering, Waseda University, 3-4-1 Okubo, Shinjuku, Tokyo 169-8555, Japan
[5] Center for Computational Astrophysics, National Astronomical Observatory of Japan, Mitaka, Tokyo 181-8588, Japan
[6] Department of Applied Physics, Fukuoka University, Fukuoka 814-0180, Japan

[7] See also Kotake et al. (2012), which includes the spherically symmetric simulations.

[8] There are other important ingredients investigated so far. The most ongoing high-profile ingredient is dimensionality of hydrodynamics (e.g. Ohnishi et al. 2006; Murphy & Burrows 2008; Nordhaus et al. 2010; Hanke et al. 2012; Couch 2013a; Takiwaki et al. 2014). As for the nuclear equation of state in multidimensional hydrodynamic modeling, see Suwa et al. (2013) and Couch (2013b). In addition, detailed neutrino interactions are also investigated in (Suwa et al. 2011; Müller et al. 2012b). Note that these studies listed above are all done using multi-dimensional simulations.

(2012) performed a systematic study for 101 progenitor models from Woosley et al. (2002) using spherically symmetric simulations with parametrized neutrino luminosity and investigated the explosion energy and final compact objects (neutron stars and black holes), which strongly depend on the initial progenitor structure. Recently, this study was followed by Nakamura et al. (2014), in which they showed 2D simulation results for these 101 progenitor models. O'Connor & Ott (2013) performed a similar systematic study based on 32 progenitor models from Woosley & Heger (2007), focusing on the compactness parameter at the bounce. They found that not the zero age main sequence (ZAMS) mass but the compactness parameter is a good measure for the neutrino evolution in the pre-explosion phase. Couch & Ott (2013) pointed out that, in addition to the density structure, initial velocity perturbations affect the hydrodynamics. They showed that model with velocity fluctuations imposed before collapse can explode more easily than those without them. Thus, it can be said that the importance of the initial condition is growing.

In this paper, we perform a series of neutrino-radiation hydrodynamic simulations in both spherical symmetry (1D) and axial symmetry (2D) for progenitors with a mass range from 12 $M_\odot$ to 100 $M_\odot$ in the main sequence phase. Then, we directly connect the hydrodynamic outcomes with the initial density structure. In addition, we construct a phenomenological model to predict the mass accretion history and neutrino luminosity using a density structure of progenitor alone. The paper opens with the description about the numerical simulations in Section 2. Then, introducing a new picture to understand supernova explosion driven by neutrino-heating mechanism in Section 3, we propose a *tuning point* combined with the so-called critical curve as a measure of successful explosion. A phenomenological model, which describes the numerical results very well, is presented in Section 4. We summarize our results and discuss their implications in Section 5.

2. NUMERICAL SIMULATIONS

2.1. *Methods*

The numerical methods are basically the same as those in our previous studies (Suwa et al. 2010, 2011, 2013; Suwa 2014). With the ZEUS-2D code (Stone & Norman 1992) as a base for the hydrodynamics solver, we employ the equation of state of Lattimer & Swesty (1991) with the incompressibility $K = 220$ MeV, for which the maximum mass of a cold NS is 2.04 $M_\odot$, i.e. more massive than the mass of recently discovered massive NSs (Demorest et al. 2010; Antoniadis et al. 2013). We solve the neutrino transfer equation for $\nu_{\rm e}$ and $\bar{\nu}_{\rm e}$ by the isotropic diffusion source approximation (IDSA) scheme (Liebendörfer et al. 2009) that splits the neutrino distribution function into two components, both of which are solved with different numerical techniques. The weak interaction rates for neutrinos are calculated according to Bruenn (1985). The simulations are performed on a grid of 300 logarithmically spaced radial zones extending up to 5000 km with the smallest grid width being 1 km at the center and 128 equidistant angular zones covering $0 < \theta < \pi$ for two-dimensional (2D) simulations. For neutrino transport, we use 20 logarithmically spaced energy bins ranging from 3 to 300 MeV.

2.2. *Progenitor Structures*

We employ progenitors calculated by Woosley & Heger (2007), who performed stellar evolutionary simulations with solar metallicity. The employed progenitors have 12, 15, 20, 30, 40, 50, 55, 80 and 100 $M_\odot$ at ZAMS. Some relevant quantities are presented in Table 1.

First, we present the structures of these models. Top two panels in Figure 1 exhibit the density structures as functions of the radius (panel (a)) and enclosed mass (panel (b)). Panel (c) shows the mass-radius relation, in which the free-fall timescales ($t_{\rm ff} = \sqrt{r^3/GM}$, where r is the radius, G is the gravitational constant, and M is the enclosed mass) are plotted as dashed lines. One can find that the density structure and ZAMS mass do not correlated with each other in a simple way: the density at the enclosed mass of 2 $M_\odot$ (see panel (b)) becomes the smallest for the model with a ZAMS mass of 12 $M_\odot$ and attains the maximum at 40 $M_\odot$. Models with the ZAMS masses larger than 40 $M_\odot$ have densities in between. This is because strong mass loss during the main sequence and giant phases yield smaller cores (see also Table 1). From dashed lines in panel (c), one can easily see that the difference of structure leads to different accretion time of mass elements, which then results in different mass accretion histories.

In Figure 2, we show the compactness parameter defined in O'Connor & Ott (2011) as

$$\xi_M = \left.\frac{M/M_\odot}{R(M)/1000\ {\rm km}}\right|_{t=t_{\rm bounce}}, \qquad (1)$$

where $R(M)$ denotes the radius for the enclosed mass M. One can find that the 12 $M_\odot$ model has the smallest ξ_M at all enclosed masses, which increases with the progenitor mass up to 40 $M_\odot$. Interestingly, the models with 50, 55, 80 and 100 $M_\odot$ have smaller ξ_M than the model with 40 $M_\odot$, which is consistent with the results of O'Connor & Ott (2013), in which they showed that the model with 40 $M_\odot$ gives the maximum values both for $\xi_{1.75}$ and $\xi_{2.5}$. In this sense the model s40 is the most compact progenitor, whereas the model s12 is the least compact one. Recently, the ξ parameter before core bounce is discussed in Sukhbold & Woosley (2014) and it is found that ξ can be a good measure to examine the progenitor structure even before the bounce.

From the next subsection we present our numerical simulations in 1D and 2D consecutively.

2.3. *Spherically symmetric simulations*

In Figure 3, we show the time evolutions of shock radius (panel (a)) and the mass accretion rates at 300 km (panel (b)). One can find that all simulations fail to explode due to insufficient neutrino heating. The evolution of shock radius is connected with the mass accretion rate, which is a good indicator for the ram pressure that determines the shock position. As for models s20, s30, s50, s55, and s80, since the mass accretion rate decreases rapidly until $\sim$ 200 ms after bounce and becomes almost stationary later on, the shock expands at $\sim$ 200 – 300 ms postbounce. The other progenitors, i.e., s12, s15, and s100, show continuous decreases in the accretion rate, with the maximum shock radius being obtained

Table 1
Properties of investigated progenitors

Model	ZAMS mass ($M_\odot$)	final mass ($M_\odot$)	final radius ($R_\odot$)	Fe core mass ($M_\odot$)	Fe core radius (1000 km)
s12	12	10.91	638.41	1.285	1.061
s15	15	12.79	831.04	1.346	1.172
s20	20	15.93	1066.68	1.540	1.591
s30	30	13.89	1552.89	1.476	1.448
s40	40	15.34	11.80	1.804	2.123
s50	50	9.82	5.42	1.487	1.489
s55	55	9.38	0.70	1.453	1.412
s80	80	6.37	0.60	1.479	1.501
s100	100	6.04	0.55	1.452	1.402

between $\sim$ 100 and 200 ms postbounce. Note that s40 is an exception, with a rapid decrease in the mass accretion rate around 500 ms postbounce, although only a small expansion of shock is observed at this time. This is because this progenitor has very large accretion rates, equivalently strong ram pressures, and the shock expansion is almost inhibited. The transition from the rapidly decreasing accretion phase to the stationary accretion phase is originated from the transition of accreting layers, i.e., from the silicon layer to the oxygen layer, where one can observe a large density jump (see Woosley & Heger 2007).

In Figure 4, we show the time evolution of each progenitor in the $\dot{M}$-L_ν plane, where $\dot{M}$ is the mass-accretion rate at 300 km and L_ν is the total neutrino luminosity (i.e. the sum of contributions of ν_e and $\bar{\nu}_e$). On these curves, each model moves from right (high-accretion rates) to left (low-accretion rates). As the mass accretion rate decreases, the neutrino luminosity also decreases. Although it seems that the neutrino luminosity declines steeply near the left end, this is just an artifact by the projection in this plane. The mass accretion rate becomes almost constant after a certain time as shown in Figure 3(b), while the neutrino luminosity continues to decrease thereafter. This point marks the transition from the dynamical accretion phase to the stationary accretion phase. Since the critical curve is a smoothly increasing function in this plane (see Burrows & Goshy 1993), the position of this point in the $\dot{M}$-L_ν plane is crucial for the shock revival. If this point locates to the top left corner in this plane (i.e., low mass accretion rates and high neutrino luminosities), such a model will be more likely to produce an explosion, particularly in multi-dimensional simulations, in which the critical curve is supposed to be lower than in the 1D case. Models s12, s55, and s80 are hence good candidates for exploding models in 2D.

Figure 5 is the same as Figure 4 but for selected models, i.e., s12, s15, s20, and s55. The other models not shown in the figure have similar trajectories. Models s20 and s55 have a clear inflection point — this point is referred to *turning point* in the next section — at $(\dot{M}, L_\nu) \approx (0.4 M_\odot\ \mathrm{s}^{-1}, 9\times10^{52}\ \mathrm{erg\ s}^{-1})$ and $\approx (0.35 M_\odot\ \mathrm{s}^{-1}, 8\times10^{52}\ \mathrm{erg\ s}^{-1})$, respectively. This is due to drastic changes in the mass accretion rate that are found in Figure 3(b). The luminosities and mass accretion rates for these models move from right to left rapidly up to the turning point and then shift downwards slowly later. They are hence expected to stay near the turning point for a long time, and that is the point, where shock revival is most likely to occur. This is why we propose to employ the position of the tuning point as a diagnostic of explosion. Although it may appear that the other models do not show a clear turning point in this figure, they actually have similar turning points at later times.

2.4. *Axially symmetric simulations*

In this subsection, we show the results of 2D simulations for the progenitors explored in the previous subsection.

Figure 6 gives time-space evolutions of entropy around north (top panels) and south poles (bottom panels). There are several oscillations in the shock radius for these models, which might be consequences of the standing accretion shock instability (SASI). It is clear that the material in the postshock region is heated up by neutrino irradiation from PNS (the yellow color represents high entropies). Thanks to long heating by neutrinos, some models (s12, s40, s55, and s80) eventually produce a shock expansion. The other models (s15, s20, s30, s50, and s100) yield no explosion at least by the end of simulations even though there is certainly neutrino heating observed.

Figure 7 presents time evolutions of the shock radius averaged over solid angle. One can find also in this figure that there are several progenitors that produce shock expansion. This is necessary condition of the supernova explosion.[9] Models with 12, 55, and 80 $M_\odot$ exhibit the shock expansion within $\lesssim$ 300–600 ms after the bounce, and the model with 40 $M_\odot$ gives a rather late onset of expansion at $\sim$ 1100 ms postbounce. These models correspond to those that realize the condition of *low mass accretion rates with high neutrino luminosities*, which is shown in Figure 4. The onset time of the shock expansion is fairly delayed from the time of the transition from the dynamical to stationary accretion phases (see Figure 3(b)) because the mass accretion rate in Figure 3(b) is evaluated at 300 km from the center and it takes some time for this transition layer to propagate toward PNS. The development of shock oscillations also needs some time.

The top panel of Figure 8 exhibits the abundance of ^{28}Si (red line) and ^{16}O (green line) as well as the den-

[9] Note that this is just a consequence of the dominance of the post-shock thermal pressure over the ram pressure in the pre-shocked region and does not imply the *successful* explosion immediately. In fact, it is still possible that the mass accretion to PNS continues and the PNS mass increases. In order to produce the *successful* explosion, the mass accretion onto PNS should stop and the envelope should move outward. See Suwa et al. (2013) for more details.

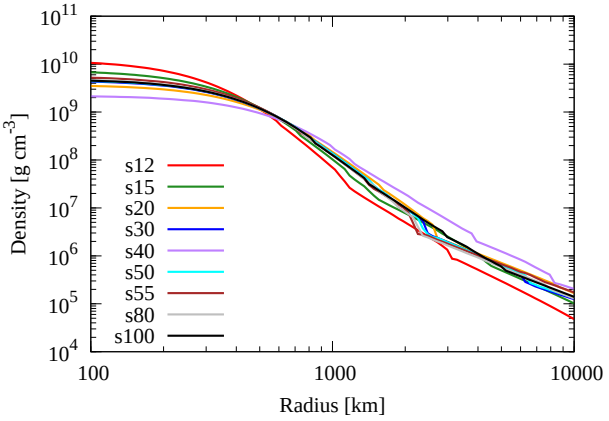

(a) Density as function of radius

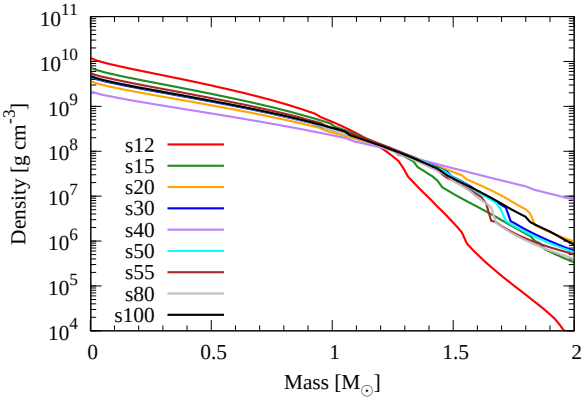

(b) Density as function of enclosed mass

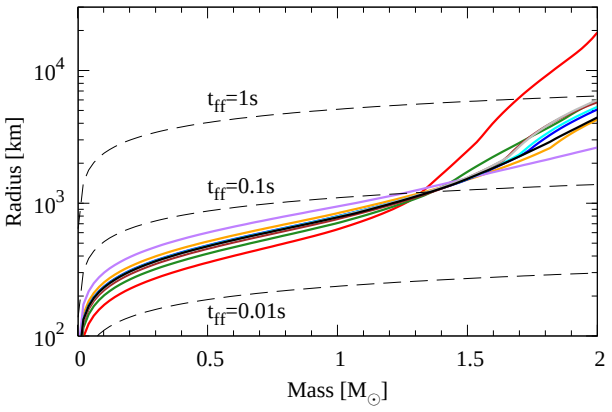

(c) Radius as function of enclosed mass

Figure 1. Stellar structures for investigated models. Top two panels display the densities as a function of radius (a) and enclosed mass (b), respectively. Bottom panel (c) give the radii corresponding to the mass and radius relations. Dashed lines show the free-fall times of 0.01, 0.1, and 1 s from bottom to top. See the text for detail.

sity (blue line). One can find that there are two density jumps at 1.66 $M_\odot$ and 2.17 $M_\odot$ in mass coordinate. The bottom panel of this figure displays as gray lines the trajectories of mass shells at the mass coordinates of 1 $M_\odot$ to 1.85 $M_\odot$ with an interval of 0.01 $M_\odot$. Three thin black lines show the representative mass coordinates of 1.66, 1.7, and 1.75 $M_\odot$. Note that 1.66 $M_\odot$ corresponds to

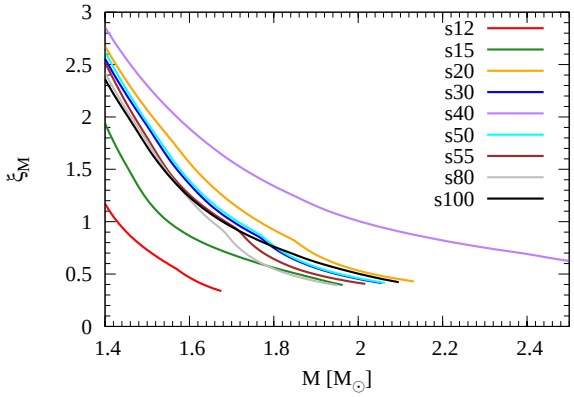

Figure 2. The *compactness* parameters ξ_M defined in Eq. (1) as a function of mass coordinate M. A lager ξ_M means a more compact structure: s12 is the least compact progenitor, while s40 is the most compact.

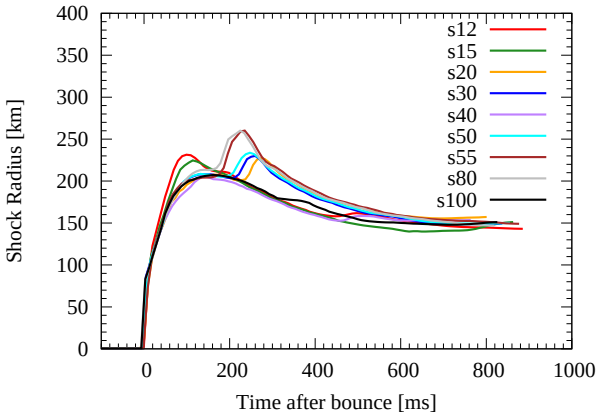

(a) Shock radius evolution

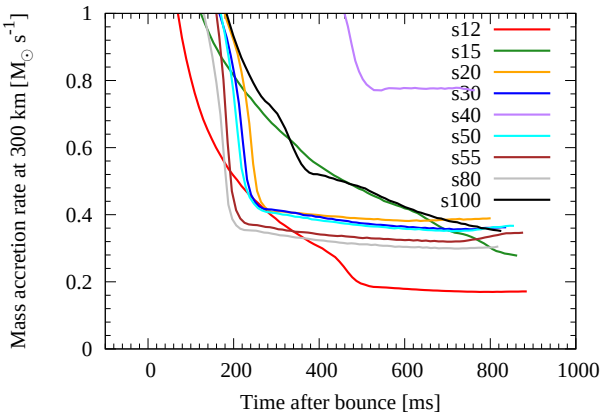

(b) Mass accretion rate evolution

Figure 3. The time evolutions of shock radius (a) and mass accretion rate (b). There are bumps in panel (a), which correspond to the rapid decreases of mass accretion rate (see panel (b)).

the interface of the oxygen burning shell (see also panel (a)). It is interesting to see what happens when this mass shell accretes onto the shock (thick black line). It is evident that several oscillations ensue and the standing shock is finally converted to the expanding shock at $\sim$ 400 ms after the bounce. This is a clear demonstration

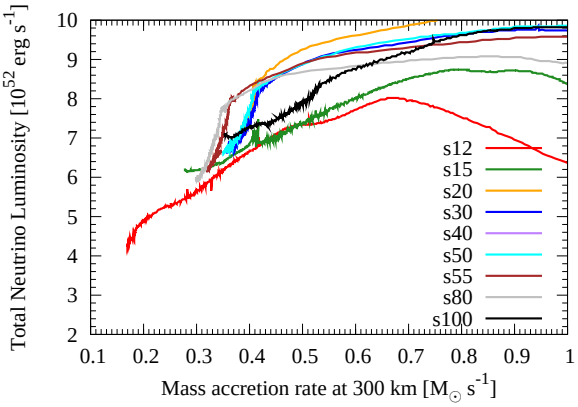

Figure 4. Model trajectories in the $\dot{M}$-L_ν plane. The mass accretion rate is evaluated at 300 km from the center.

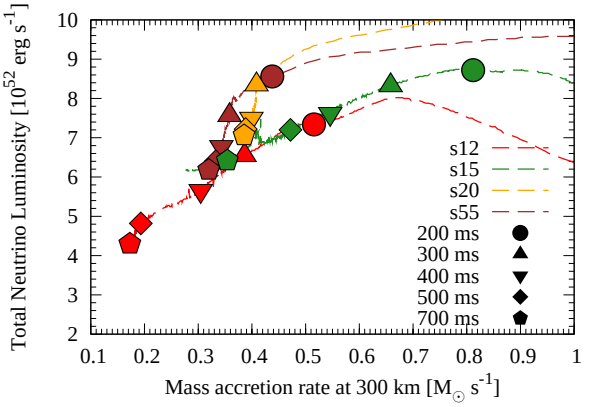

Figure 5. Model trajectories in the $\dot{M}$-L_ν plane for selected models with various points representing the times after bounce. The colors of lines are the same as those in Figure 4. Each model evolves from right to left.

that the transition of accretion phases leads to the phase transition in shock evolution due to the drastic change in the mass accretion rate.

In Figure 9, we show the so-called diagnostic energy, which is defined as the integral of the sum of specific internal, kinetic and gravitational energies over all zones, in which it is positive. Four exploding models (s12, s40, s55 and s80) have indeed non-vanishing diagnostic energies. Some oscillations originate from the shock oscillations. Though the diagnostic energy is gradually increasing, the final value is still much smaller than the typical value of observed explosion energy, $\sim 10^{51}$ erg. Although even nonexploding models have positive diagnostic energies due to neutrino heating, it is insufficient to revive the stalled shock wave.

2.5. $15M_\odot$ *stars*

In this subsection, we focus on different progenitors with the same typical mass of $15M_\odot$ at ZAMS. In addition to model s15 just studied, we use four more models from Nomoto & Hashimoto (1988) (NH88), Woosley & Weaver (1995) (WW95), Woosley et al. (2002) (WHW02), and Limongi & Chieffi (2006) (LC06). First three of them were employed in Suwa et al. (2011), in which neutrino oscillation effects on the supernova explosion were investigated. The pre-collapse density structures are given in Figure 10 (see also Figure 8 of Suwa et al. 2011 for comparison of the density structures at 100 ms after the bounce. It was discussed in that paper that the structures are similar among the different models for $M < 0.8M_\odot$ whereas they are different for $M > 0.8M_\odot$). One can find that even though the initial mass at ZAMS is the same, the density structures prior to collapse become different, depending on both physics and numerics implemented in stellar evolutionary calculations. It should be noted in particular that difference between WW95 and WH07 is substantial at 1500–2000 km before collapse (see Figure 10).

Figure 11 presents model trajectories in the $\dot{M} - L_\nu$ plane evaluated for the 1D simulations, which is the same as Figure 4 but for the present models. One can find that NH88 and WW95 are likely to achieve conditions more suitable for explosion, i.e., larger neutrino luminosities combined with smaller accretion rates. This is a consequence of the density jump observed in Figure 10. Note, however, that all 1D simulations failed to produce explosion.

The shock evolutions for the 2D simulations are given in Figure 12, in which two progenitors (NH88 and WW95) appear to succeed in producing shock expansions. It is hence clear that even if the ZAMS mass is the same, the outcome in the shock evolution can be completely different, depending on the treatment of physics (e.g., convection, semiconvection, overshooting, and stellar wind) and numerics in stellar evolution calculations. It is obvious that progenitors realizing high neutrino luminosities with low mass accretion rates as seen in Figure 11 are better for explosion. This is the same conclusion as in the previous subsection.

3. CRITICAL CURVE AND TURNING POINT

In this section, we propose a novel method to diagnose a possibility of explosion using the $\dot{M}$-L_ν plane (see Figure 13). This plane is often used to discuss the critical curve, which divides this plane into two regions: in the region below this line there are steady accretion flows, while in the other region above this line there is no such flow (Burrows & Goshy 1993). The latter is hence interpreted as the region, where shock revival occurs. Then, the trajectory in this plane will be a good diagnostic measure to examine the possibility of explosion.

In Figure 13, we present a schematic picture of the trajectory and the critical curve in the $\dot{M}$-L_ν plane. The red solid line represents the critical curve and the black dotted line gives a typical model trajectory. As demonstrated already, the point in this drawing is that there is a transition point in the trajectory, which implies a drastic change in L_ν as a function of $\dot{M}$. This point is referred to as the *turning point* in this paper. If the turning point is located above the critical curve and the luminosity and mass accretion rate stay there for a long time, such a model will be highly likely to produce explosion.

It is obvious that the combination of a lower critical curve and a higher turning point is preferred for supernova explosion. Multi-dimensionality of supernova dynamics has been demonstrated to lower the critical curve (Murphy & Burrows 2008; Nordhaus et al. 2010; Hanke et al. 2012). The impact of properties of the nuclear equation of state on the critical curve is also studied

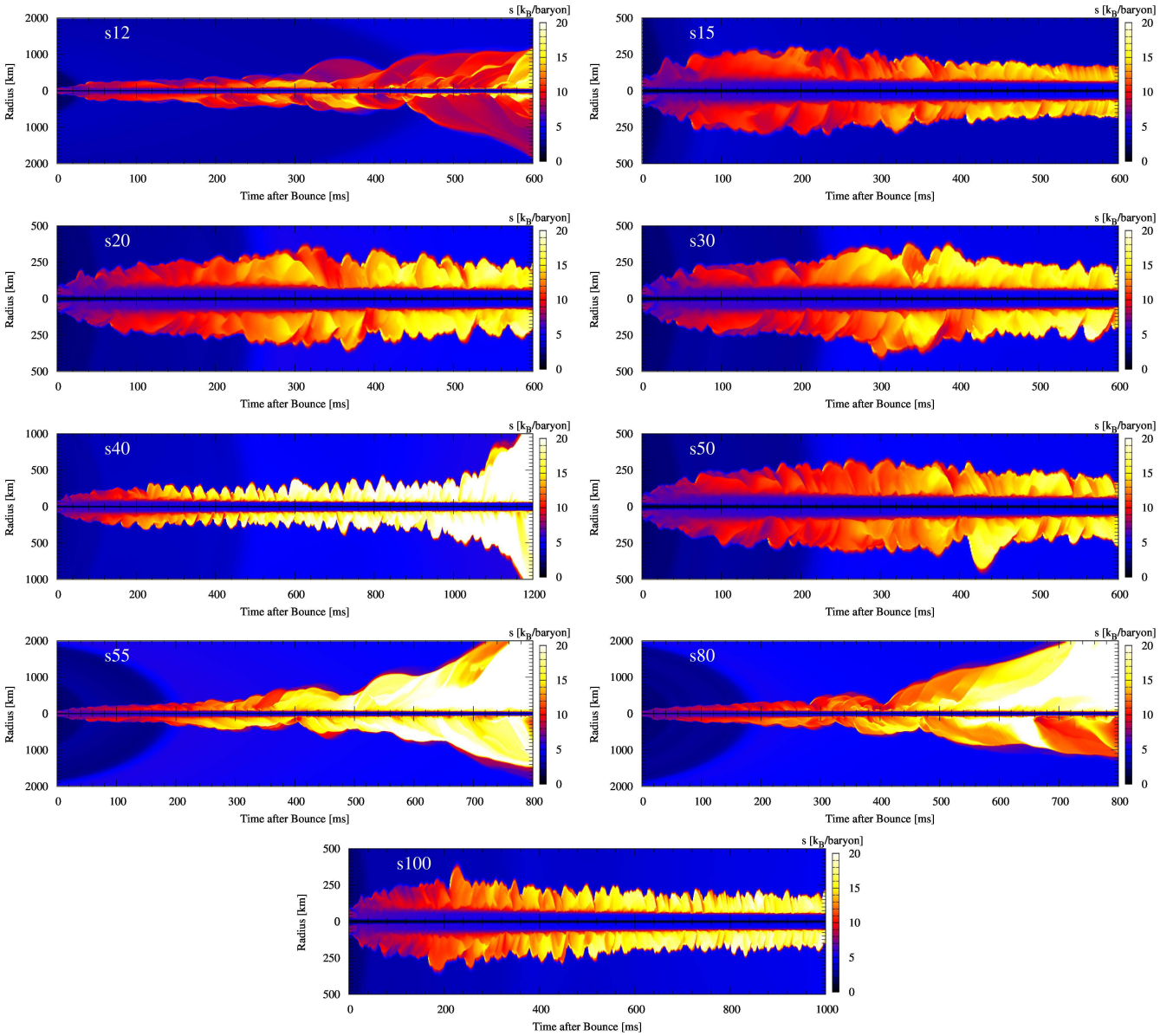

Figure 6. Time-space diagrams of specific entropy at poles for two-dimensional simulations. Upper (lower) panels represent the values at the north (south) pole. Models s12, s40, s55, and s80 eventually produce explosion at different times, depending on the initial density structures. The other progenitors, i.e., s15, s20, s30, s50, and s100, failed to produce explosion at least by the end of simulations.

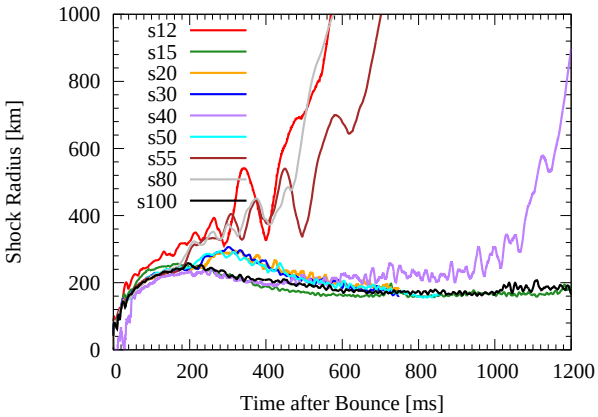

Figure 7. Time evolutions of the angle averaged shock wave radius. Four of the investigated models, i.e. s12, s40, s55 and s80, clearly show shock expansions.

(Couch 2013b) and is found to be minor compared to the dimensionality.[10] Although the critical curve has been well studied by several groups, we emphasize that we should study the trajectory as well. In so doing, however, neutrino-radiation hydrodynamic simulations, or *ab initio* computations with detailed neutrino physics and radiative transfer being incorporated are indispensable to obtain reliable model trajectories. It is also noted that the model trajectory is useful to discuss to what extent particular ingredients included in simulations (e.g., the nuclear equation of state, neutrino interactions, scheme to solve the neutrino transfer equation) affect the shock dynamics. The dependence of the location of the turning point on them is especially crucial.

In the following, based on results of the neutrino-

[10] There are a few attempts to derive the critical curve analytically (Pejcha & Thompson 2012; Keshet & Balberg 2012).

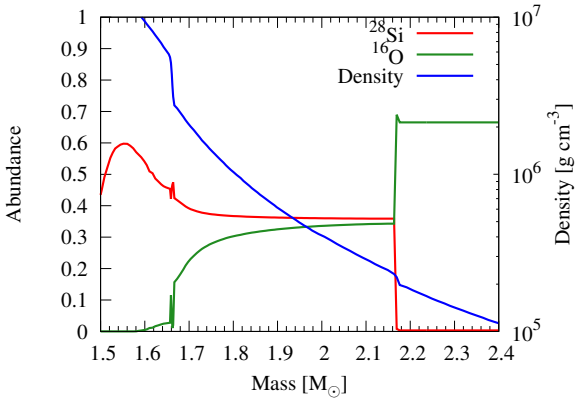

(a) Abundance distribution and density structure

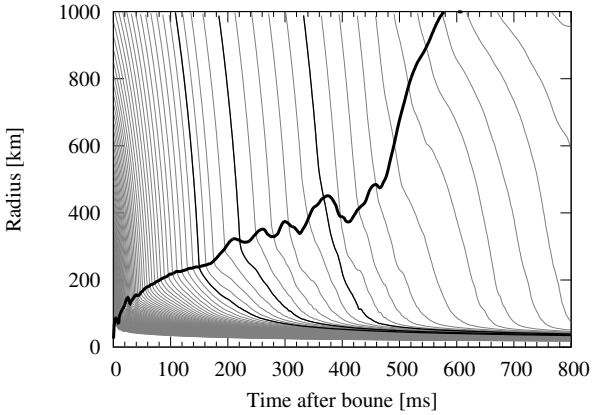

(b) Time evolution of mass coordinate and shock

Figure 8. (Top) The initial profiles of density and composition for model s80. The abundance of ^{28}Si (red line) and ^{16}O (green line), and the density (blue line) are given as a function of mass coordinate. There are two jumps in density, representing the transition of layers. (Bottom) Trajectories of the mass shells with the mass coordinates of 1 $M_\odot$ to 1.85 $M_\odot$ with an interval of 0.01 $M_\odot$ are plotted as grey curves for the same model. Thin black lines represent 1.66, 1.7, and 1.75 $M_\odot$ from left to right, respectively. A thick black curve indicates the average shock position. When the mass shell of 1.66 $M_\odot$ runs across the shock several oscillations ensue in the shock radius. The shock is eventually expanded at $\sim$ 400 ms after the bounce.

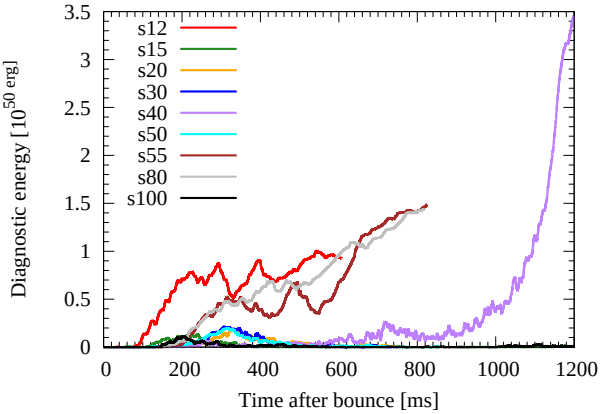

Figure 9. Time evolutions of the diagnostic energy for 2D models. It is defined by the integral of the sum of the specific internal, kinetic, and gravitational energies, over the zones, in which it is positive. The horizontal axis is the postbounce time.

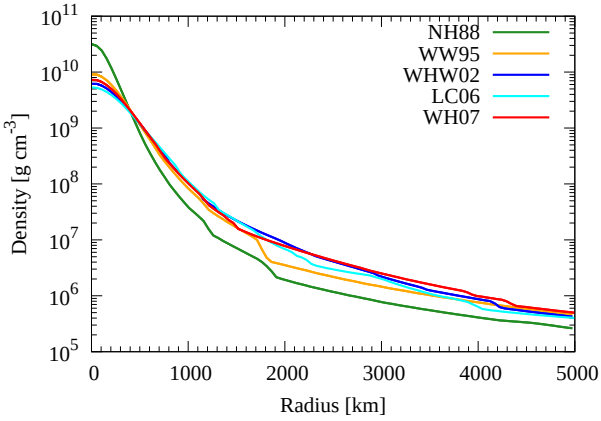

(a) Density as a function of radius

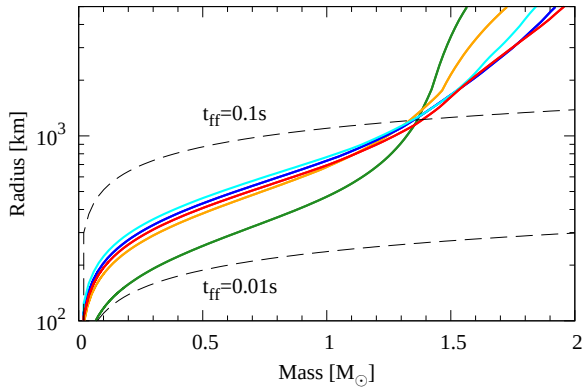

(b) Radius as a function of enclosed mass

Figure 10. The same as Figure 1 but for progenitors with the ZAMS mass of 15 $M_\odot$. Here we use five models from Nomoto & Hashimoto (1988) (NH88), Woosley & Weaver (1995) (WW95), Woosley et al. (2002) (WHW02), Limongi & Chieffi (2006) (LC06), and Woosley & Heger (2007) (WH07). Due to the different treatments of physics and numerics for stellar evolutionary calculations, the structures prior to collapse show diversity even if they have the same ZAMS mass. In the bottom panel, free-fall times are given by dashed lines.

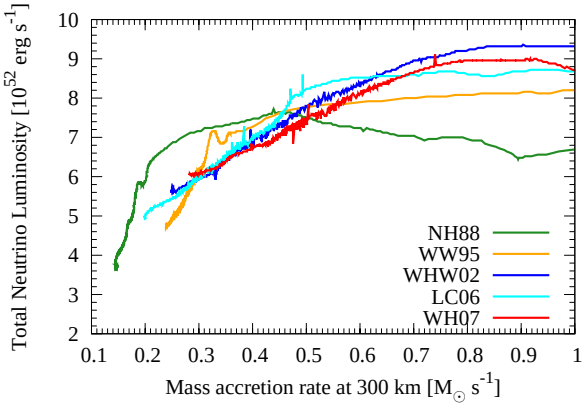

Figure 11. Model trajectories in the $\dot{M} - L_\nu$ plane for the 1D simulations of 15 $M_\odot$ progenitors. This is the same as Figure 4 but for different progenitor models. The mass accretion rate is evaluated at 300 km from the center.

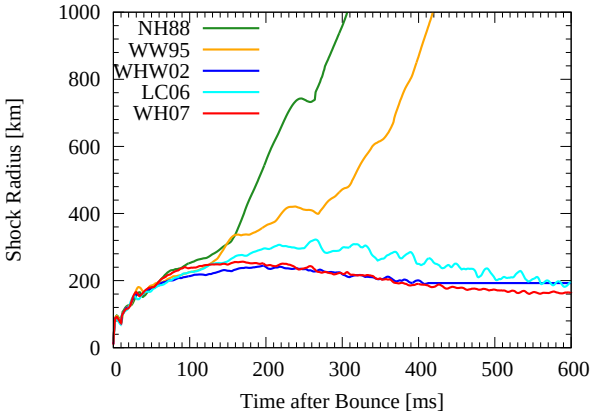

Figure 12. Time evolutions of the angle-averaged shock radius for 15 $M_\odot$ progenitors. NH88 and WW95 produce explosion owing to small densities of the envelopes.

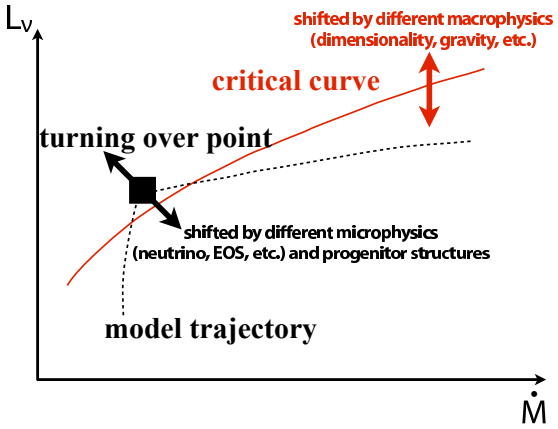

Figure 13. Schematic picture of the critical curve and turning point. If the turning point is located above the critical curve and the luminosity and mass accretion rate stay in the vicinity of the tuning point for a long time, such a model will produce explosion. The critical curve is expected to be shifted by macrophysics such as dimensionality and the turning point may be shifted by microphysics as well as the progenitor structure. The critical curve and turning point are also useful to asses the influence of a particular physics incorporated.

radiation hydrodynamic simulations presented so far, we develop a phenomenological model that connects the density structure of progenitor just prior to collapse and the model trajectory in the $\dot{M}$-L_ν plane.

4. PHENOMENOLOGICAL MODEL

In this section, we construct a phenomenological model to estimate the neutrino luminosity as a function of the mass accretion rate from the density structure of progenitor.

In this model the mass accretion rate is evaluated a

$$\dot{M} = \frac{dM}{dt_{\rm ff}} \tag{2}$$

$$= \frac{dM}{dr}\left(\frac{dt_{\rm ff}}{dr}\right)^{-1}, \tag{3}$$

where $t_{\rm ff}$ is the free-fall time, which is defined as a function of the radius by

$$t_{\rm ff} = \alpha\sqrt{\frac{r^3}{GM}}$$

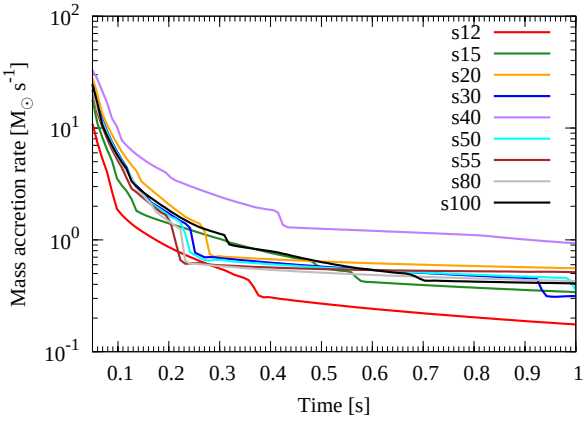

Figure 14. Mass accretion rate calculated by the free-falling model.

$$\approx 0.130\ {\rm s}\left(\frac{\alpha}{1.5}\right)\left(\frac{r}{1000\ {\rm km}}\right)^{3/2}\left(\frac{M}{M_\odot}\right)^{-1/2}, \tag{4}$$

where α is a parameter introduced to adjust to numerical result. Inverting this relation, we regard the radius as a function of $t_{\rm ff}$ in Eq. (3). Figure 14 shows the mass accretion rates as a function of t, which is identification with $t_{\rm ff}$, for the progenitor models investigated in this paper. The figure should compared with the bottom panel of Figure 3 (note that the vertical scale is different.). It is seen that the the mass accretion rates are high and rapidly decreasing at first. When the silicon layer fully accretes to a PNS, the mass accretion rates become smaller significantly because of the density drop at the layer boundary and remain almost constant thereafter.

Although there have been several approximate functional forms, e.g. $e^{-t/\tau}$ (Janka & Mueller 1996), proposed for the total neutrino luminosity as a function of time, we employ the following form based on the diffusion time scale:

$$L_\nu(t) = \frac{L_{\rm diff}}{1 + t/t_{\rm diff}}, \tag{5}$$

where $L_{\rm diff} = E_{\rm int}/t_{\rm diff}$ is the diffusion luminosity with $E_{\rm int} = (3/5)GM_{\rm PNS}^2/R_\nu$ being the internal energy stored inside a PNS and $t_{\rm diff}$ being the diffusion timescale defined shortly later, and $M_{\rm PNS}$ and R_ν are the mass and the radius of the PNS. Again identifying $t_{\rm ff}$ with t, we get the following expression,

$$L_\nu = \frac{E_{\rm int}}{t_{\rm ff} + t_{\rm diff}}. \tag{6}$$

The diffusion time $t_{\rm diff}$ can be evaluated as (see Appendix for the derivation)

$$t_{\rm diff} = \frac{3\sigma}{4\pi c m_{\rm p}}\frac{M}{R_\nu}$$

$$\approx 0.402\ {\rm s}\left(\frac{\varepsilon_{\nu,{\rm PNS}}}{57\ {\rm MeV}}\right)^2\left(\frac{M}{M_\odot}\right)\left(\frac{R_\nu}{50\ {\rm km}}\right)^{-1}, \tag{7}$$

where σ is the cross section of neutrino-nucleon scattering, which is given as $\sigma(\varepsilon_\nu) \approx \sigma_0(\varepsilon_\nu/m_{\rm e}c^2)^2$ with $\sigma_0 = 1.705\times10^{-44}$ cm^2,[11] the electron mass $m_{\rm e}$, and

[11] There are coefficients of $O(1)$, which are neglected for sim-

the neutrino energy ε_ν. The proton mass is denoted by $m_{\rm p}$. Additionally, $\varepsilon_{\nu,{\rm PNS}}$ is a characteristic energy of neutrinos inside the PNS.[12] The mass of PNS increases as matter accretes and can be expressed as a function of time by the use of the free fall time.

The idea that underlies Eq. 7 is the following. The material that is initially located at r falls onto the PNS in its free-fall time; the gravitational energy is then converted to the internal energy, which is finally radiated as neutrinos in the diffusion time. We can then evaluate the neutrino luminosity as Eq. (6). This phenomenological model is consistent with the fact that the neutrino luminosity seems to be regulated by the smaller of the accretion and diffusion luminosities (Fischer et al. 2009; Mueller & Janka 2014). In fact, since $L_{\rm acc} \sim E_{\rm int}/t_{\rm ff}$ and $L_{\rm diff} \sim E_{\rm int}/t_{\rm diff}$. It follows that $L_{\rm acc} < L_{\rm diff}$ for $t_{\rm ff} > t_{\rm diff}$, and vise versa.

Figure 15 represents the model trajectories in the $\dot{M}$-L_ν plane obtained this way. In this plot, we employ $\alpha = 1.5$, $\varepsilon_{\nu,{\rm PNS}} = 57$ MeV, and $R_\nu = 50$ km in Equations (4) and (7). The comparison between the phenomenological model and the numerical results is given in Appendix B (see Fig. 17). Filled squares shown in Figure 15 represent the points on each trajectory, which will be the most favorable for the explosion and are determined so that the maximum value of the ratio of the calculated L_ν to the critical luminosity given by Burrows & Goshy (1993) as

$$L_{\rm BG}^{\rm crit} = 5\times10^{52}{\rm erg\ s^{-1}}\left(\frac{\dot{M}}{1.1\ M_\odot\ {\rm s^{-1}}}\right)^{1/2.3} \quad (8)$$

should be maximum. Note that, strictly speaking, Eq. (8) is valid only for the luminosity of electron-type neutrino, L_{ν_e}, with the temperature of $kT_{\nu_e} = 4.5$ MeV. Here the Boltzmann constant is denoted by k. We believe, however, that it will not be so bad for the current purpose. One can find that the filled squares coincide with the turning points, where the $\dot{M}$-L_ν relation changes drastically. For example, for model s12, this point occurs at $\dot{M} \approx 0.2 M_\odot$ s^{-1} and L_ν is a rapidly increasing function of $\dot{M}$ for larger mass accretion rates whereas it increases rather slowly for smaller mass accretion rates. As mentioned repeatedly this drastic change comes from the transition of accreting layers from silicon to oxygen layers.

In Figure 16 the locations of the turning points for different models are plotted as open circles for exploding models and as crosses for nonexploding models in 2D simulations given in Section 2.4. The dashed line is given by $L_\nu = 13\times10^{52}{\rm erg\ s^{-1}}(\dot{M}/1.1\ M_\odot\ {\rm s^{-1}})^{1/2.3}$, which seems to divide the exploding models from the nonexploding ones. Note that s20 does not meet this condition because we do not take into account the dependence of the critical curve on the average energy of emitted neutrinos and PNS mass (see, e.g., Pejcha & Thompson 2012). We do not make an attempt to improve it here to avoid further complications. We stress, however, that it is evident from the figure that the comparison of the turning point with the critical curve is useful to predict the possibility of explosion from the progenitor structure alone.

plicity (see Burrows et al. 2006, for more details).

[12] The characteristic value employed here seems rather large compared with the commonly used one ~ 10 MeV. This is because the former represents the average energy inside the PNS, where the matter temperature is $O(10)$ MeV and, as a consequence, the neutrino average energy is also $O(10)$ MeV. On the other hand, the latter value reflects the matter temperature at the neutrinosphere, $O(1)$ MeV.

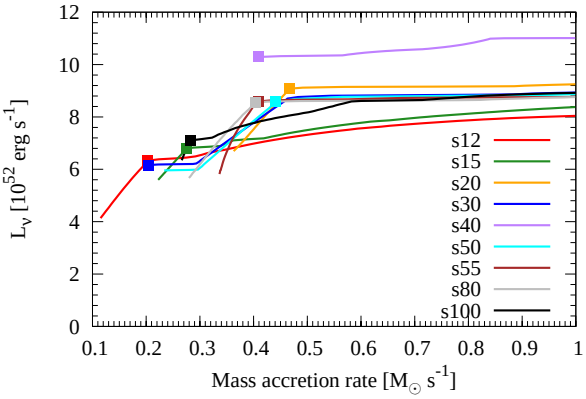

Figure 15. Phenomenological model for neutrino luminosity as a function of mass accretion rate.

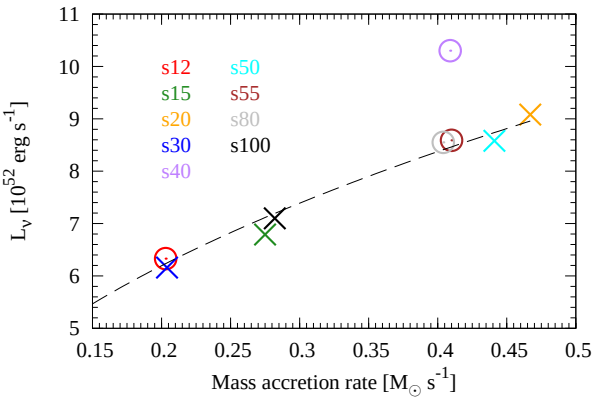

Figure 16. The location of turning points of investigated models are represented as open circles for exploding models and crosses for nonexploding models in 2D simulations given in Section 2.4. Dashed line is $L_\nu = 13\times10^{52}{\rm erg\ s^{-1}}(\dot{M}/1.1\ M_\odot\ {\rm s^{-1}})^{1/2.3}$, which seems to divide the phase space into exploding and non-exploding regions.

Murphy & Burrows (2008) provided $L_\nu \approx 10\times10^{52}{\rm erg\ s^{-1}}(\dot{M}/1.1\ M_\odot\ {\rm s^{-1}})^{1/2.3}$ as their critical curve based on their 1D simulations, which is already lower than our critical curve, and the critical luminosities in 2D are even smaller as shown in their Figure 17. This discrepancy should be ascribed to the different treatments of neutrino transfer. We suspect that the overestimations of neutrino luminosities and, as a consequence, of neutrino heating at late times in the simple approximation are responsible for the discrepancy.

5. SUMMARY AND DISCUSSIONS

In this paper, we performed neutrino-radiation hydrodynamic simulations in spherical symmetry (1D) and

axial symmetry (2D) for different progenitor models by Woosley & Heger (2007) from 12 $M_\odot$ to 100 $M_\odot$. We found that all 1D runs failed to produce explosion and several 2D runs succeeded. The difference in the shock evolutions can be ascribed to different mass accretion histories, which are determined by the density structures of progenitors. The exploding models have in common *high neutrino luminosities and low mass accretion rates*. This is consistent with the criterion based on the critical curve, above which there is no steady accretion flow and shock revival is expected. In addition, we developed a phenomenological model to estimate trajectories in the $\dot{M}$-L_ν plane. This model reproduces the numerical results reasonably well by using the initial density structures of progenitor alone. With this model, we can predict the possibility of explosion without detailed simulations.

Our results also suggest a new methodology to compare different simulation codes of neutrino-radiation hydrodynamics for the supernova explosion in the context of the neutrino heating mechanism. Interestingly, the results obtained by these codes do not agree with each other and comparative studies are much required (see Liebendörfer et al. 2005, for comparison of 1D simulations). We propose to employ the trajectory in the $\dot{M}$-L_ν plane for comparison. The methodology can be also used to gauge the effects of particular physical processes, i.e., to see how the trajectory is shifted using 1D simulations.

At last, we comment on the assumptions adopted in this study. Firstly, we performed 2D simulations although it is well known that axial symmetry leads to some hydrodynamic features that are qualitatively different from those in three dimensions (3D) (Couch 2013a; Hanke et al. 2013; Handy et al. 2014; Takiwaki et al. 2014). The critical curve in 3D is shifted from that in 2D (Nordhaus et al. 2010; Hanke et al. 2012) although the magnitude and its dependence on the spacial resolution is still controversial. We believe, however, that the qualitative features in this study will not change even for 3D models although they are quantitatively sensitive to details of convection and standing accretion shock instability. Incidentally,, at the moment 3D hydrodynamic simulations with spectral neutrino transfer are still computationally too expensive to perform a systematic study like the one in this paper. Secondly, the microphysics used in this study is not so elaborate as other numerical studies (Müller et al. 2012b; Bruenn et al. 2013) and our critical curve may be different from theirs. This might be the reason for the different outcomes that Bruenn et al. (2013) obtained for the same progenitor series: they found explosion for all the progenitors from 12 to 25 $M_\odot$ progenitors whereas we produced explosion only for the 12 $M_\odot$ model. The phenomenological model we proposed in this paper should be improved using more sophisticated numerical simulations, which will be done as a future project.

We thank A. Heger, M. Limongi, and K. Nomoto for providing progenitor models and M. Tanaka for fruitful discussion. Numerical computations in this study were in part carried on XT4 and XC30 at CfCA in NAOJ and SR16000 at YITP in Kyoto University. This study was supported in part by the Grant-in-Aid for Scientific Research (Nos. 25103511, 26870823, 23540323, 23340069, 24103006, 26707013, and 24244036), JSPS postdoctoral fellowships for research abroad, MEXT SPIRE, and JICFuS.

APPENDIX

A. DIFFUSION TIMESCALE

Here, we obtain a useful expression of the diffusion timescale for neutrinos in a uniform density sphere of radius R_ν, which is meant to be a rough approximation to a PNS. The diffusion timescale is given by

$$t_{\rm diff} = \frac{\tau_\nu R_\nu}{c}, \tag{A1}$$

where τ_ν is the optical depth of the sphere, which is

$$\tau_\nu = \int_0^{R_\nu} dr \frac{\rho\sigma}{m_{\rm p}} \tag{A2}$$

$$= \frac{3\sigma}{4\pi m_{\rm p}} \frac{M}{R_\nu^2}. \tag{A3}$$

Here we used $M = 4\pi\rho R_\nu^3/3$. By combining Eqs. (A1) and (A3), we get

$$t_{\rm diff} = \frac{3\sigma}{4\pi c m_{\rm p}} \frac{M}{R_\nu}. \tag{A4}$$

B. COMPARISON BETWEEN PHENOMENOLOGICAL AND NUMERICAL MODELS

In this section, we show the comparison between the phenomenological model introduced in Section 4 and the numerical results presented in Section 2.3. Figure 17 presents the model trajectories for models s12, s20, and s80. Solid curves show the model trajectories obtained with the phenomenological models and dashed curves display the trajectories given by the numerical simulations. One can find that for s80 these lines agree very well, while for s12 the phenomenological model fails to reproduce the numerical result. As for s20, there is a discrepancy between two lines at high mass accretion rates, whereas the turning point is almost perfectly reproduced. For models s30, s50, and s55, which have clear turning points in the simulations they are reproduced reasonably well by the phenomenological model. It fails, however, for models s15, s40, and s100. These results indicate that the phenomenological model is useful for progenitors that have clear turning points, i.e., progenitors with a large density jump between the silicon and oxygen layers.

C. OTHER PROGENITORS

We show the turning points for all 32 progenitors from Woosley & Heger (2007) in Figure 18. The turning point is defined for each model to be the point in the $\dot{M}$-L_ν plane, at which the ratio of $L_\nu/L_{\rm BG}^{crit}$ takes the maximum value on the trajectory. The values of $\max(L_\nu/L_{\rm BG}^{\rm crit})$ at the turning points are summarized in Table 2, in which the compactness parameters $\xi_{1.5}$, $\xi_{1.75}$, and $\xi_{2.5}$ at the precollapse phase are also given (see Sukhbold & Woosley 2014 for the relations of these quantities with the compactness parameters defined at the bounce). Note that these parameters can be also evaluated only from the density structure of progenitor and no simulation is required.

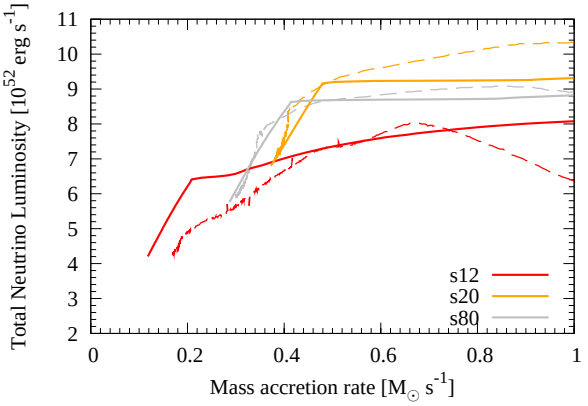

Figure 17. Comparison between numerical simulation (dashed lines) and phenomenological model (solid lines) for selected models.

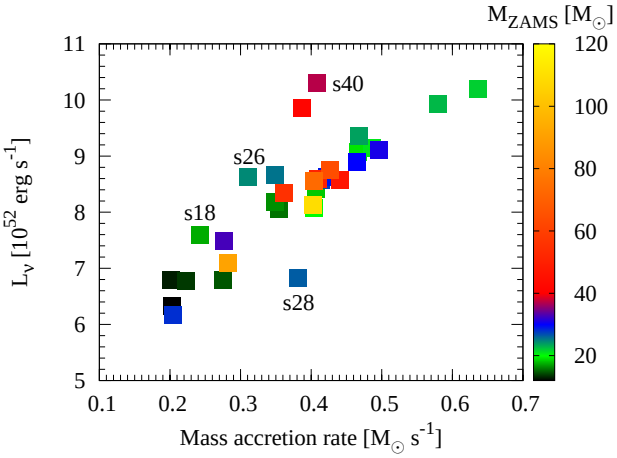

Figure 18. The location of turning points for all progenitor models of Woosley & Heger (2007), with color bar denoting the ZAMS mass. The typical progenitor models are labeled.

There is no clear correlation between the maximum values of $(L_\nu/L_{\rm BG}^{\rm crit})$ and the compactness parameters. The critical value of $\max(L_\nu/L_{\rm BG}^{\rm crit})$ that divides exploding from non-exploding models may be set at is ~ 2.18 because models s55 and s80 ($\max(L_\nu/L_{\rm BG}^{\rm crit})$=2.19) explode, while s20 ($\max(L_\nu/L_{\rm BG}^{\rm crit})$=2.18) fails. It is hence true that $\max(L_\nu/L_{\rm BG}^{\rm crit})$ is very useful in judging whether a particular model is likely to explode before doing detailed simulations.

D. CONDITIONS FOR CONSTANT $\dot{M}$

In this section, we give a simple explanation of why we obtain almost constant mass accretion rates at late times for most of the progenitors in this study. We assume the following density structure,

$$\rho(r) = \rho_0 \left(\frac{r}{R}\right)^{-n}, \tag{D1}$$

where R is a core radius and ρ_0 is the density at $r = R$. The mass coordinate is given by

$$M(r) = M_0 + \int_R^r 4\pi r'^2 \rho(r') dr', \tag{D2}$$

Table 2
Properties of all progenitors

Model	ZAMS mass ($M_\odot$)	$\max(L_\nu/L_{\rm BG}^{\rm crit})$	$\xi_{1.5}^{\rm pre}$	$\xi_{1.75}^{\rm pre}$	$\xi_{2.5}^{\rm pre}$
s12	12	2.19	0.617	0.235	0.023
s13	13	2.36	0.869	0.370	0.067
s14	14	2.25	0.857	0.502	0.128
s15	15	2.06	0.882	0.549	0.181
s16	16	2.19	0.792	0.333	0.150
s17	17	2.24	0.877	0.374	0.168
s18	18	2.43	0.961	0.656	0.194
s19	19	2.15	0.962	0.517	0.177
s20	20	2.18	1.003	0.771	0.286
s21	21	2.07	0.696	0.323	0.143
s22	22	2.16	1.001	0.783	0.289
s23	23	2.14	0.998	0.870	0.434
s24	24	2.17	1.013	0.859	0.398
s25	25	2.25	1.008	0.821	0.331
s26	26	2.48	0.968	0.641	0.234
s27	27	2.37	0.993	0.677	0.257
s28	28	1.79	0.987	0.596	0.272
s29	29	2.17	0.965	0.534	0.225
s30	30	2.13	1.006	0.688	0.218
s31	31	2.17	0.995	0.617	0.219
s32	32	2.15	0.999	0.750	0.253
s33	33	2.14	1.003	0.783	0.284
s35	35	2.26	1.010	0.846	0.360
s40	40	2.62	0.980	0.876	0.547
s45	45	2.58	0.982	0.875	0.516
s50	50	2.12	0.999	0.643	0.222
s55	55	2.19	0.980	0.564	0.239
s60	60	2.24	0.939	0.451	0.175
s70	70	2.20	0.989	0.663	0.233
s80	80	2.19	0.965	0.550	0.210
s100	100	2.13	0.989	0.702	0.245
s120	120	2.09	0.911	0.454	0.171

where M_0 is the mass coordinate at $r = R$. Then, mass accretion rate is estimated as

$$\dot{M} = \frac{dM}{dt_{\rm ff}} = \frac{dM}{dr}\left(\frac{dt_{\rm ff}}{dr}\right)^{-1}, \tag{D3}$$

where $t_{\rm ff} = \sqrt{r^3/GM(r)}$ is the free fall timescale. Short calculations give

$$\frac{dM}{dr} = 4\pi r^2 \rho_0 \left(\frac{r}{R}\right)^{-n}, \tag{D4}$$

and

$$\frac{dt_{\rm ff}}{dr} = \frac{1}{2}\sqrt{\frac{r}{GM(r)}}\left\{3 - 4\pi r^2 \rho_0 \left(\frac{r}{R}\right)^{-n}\frac{r}{M(r)}\right\}^{-1}. \tag{D5}$$

Suppose that $M(r) \approx M_0$, i.e., the central accelerator's mass is dominant and $r \gg R$. Then, $dt_{\rm ff}/dr \approx (3/2)\sqrt{r/GM(r)}$ and we obtain becomes

$$\dot{M} \approx \frac{8\pi\rho_0 R^n \sqrt{GM_0}}{3} r^{\frac{3}{2}-n}, \tag{D6}$$

which becomes constant if $n = 3/2$. On the other hand, if the mass at $r > R$, that is the mass of accreting matter, is dominant, we get

$$M(r) \approx \frac{4\pi\rho_0 R^n}{3-n} r^{3-n}, \tag{D7}$$

which leads to

$$\frac{dt_{\rm ff}}{dr} \approx \frac{n}{2}\sqrt{\frac{3-n}{4\pi G\rho_0 R^n}}r^{\frac{n}{2}-1}. \quad \text{(D8)}$$

Then we obtain

$$\dot{M} \approx \frac{2}{n}\sqrt{\frac{(4\pi\rho_0 R)^3 G}{3-n}}r^{3-\frac{3}{2}n}, \quad \text{(D9)}$$

which is again constant for $n = 2$. The progenitor models used in this study realize $n \approx 2$ for the oxygen layer so that the latter case is valid for them.

REFERENCES

Antoniadis, J., et al. 2013, Science, 340, 448
Bruenn, S. W. 1985, ApJS, 58, 771
Bruenn, S. W., et al. 2013, ApJ, 767, L6
Buras, R., Rampp, M., Janka, H.-T., & Kifonidis, K. 2006, A&A, 447, 1049
Burrows, A., & Goshy, J. 1993, ApJ, 416, L75
Burrows, A., Reddy, S., & Thompson, T. A. 2006, Nuclear Physics A, 777, 356
Couch, S. M. 2013a, ApJ, 775, 35
—. 2013b, ApJ, 765, 29
Couch, S. M., & Ott, C. D. 2013, ApJ, 778, L7
Demorest, P. B., Pennucci, T., Ransom, S. M., Roberts, M. S. E., & Hessels, J. W. T. 2010, Nature, 467, 1081
Dolence, J. C., Burrows, A., & Zhang, W. 2014, ArXiv e-prints
Fischer, T., Whitehouse, S. C., Mezzacappa, A., Thielemann, F.-K., & Liebendörfer, M. 2009, A&A, 499, 1
Handy, T., Plewa, T., & Odrzywołek, A. 2014, ApJ, 783, 125
Hanke, F., Marek, A., Müller, B., & Janka, H.-T. 2012, ApJ, 755, 138
Hanke, F., Müller, B., Wongwathanarat, A., Marek, A., & Janka, H.-T. 2013, ApJ, 770, 66
Janka, H., & Mueller, E. 1996, A&A, 306, 167
Keshet, U., & Balberg, S. 2012, Physical Review Letters, 108, 251101
Kitaura, F. S., Janka, H., & Hillebrandt, W. 2006, A&A, 450, 345
Kotake, K., Takiwaki, T., Suwa, Y., Iwakami Nakano, W., Kawagoe, S., Masada, Y., & Fujimoto, S.-i. 2012, Advances in Astronomy, 2012
Lattimer, J. M., & Swesty, F. D. 1991, Nuclear Physics A, 535, 331
Liebendörfer, M., Mezzacappa, A., Thielemann, F.-K., Messer, O. E., Hix, W. R., & Bruenn, S. W. 2001, Phys. Rev. D, 63, 103004
Liebendörfer, M., Rampp, M., Janka, H.-T., & Mezzacappa, A. 2005, ApJ, 620, 840
Liebendörfer, M., Whitehouse, S. C., & Fischer, T. 2009, ApJ, 698, 1174
Limongi, M., & Chieffi, A. 2006, ApJ, 647, 483
Marek, A., & Janka, H. 2009, ApJ, 694, 664
Mueller, B., & Janka, H.-T. 2014, arXiv:1402.3415
Müller, B., Janka, H.-T., & Heger, A. 2012a, ApJ, 761, 72
Müller, B., Janka, H.-T., & Marek, A. 2012b, ApJ, 756, 84
Murphy, J. W., & Burrows, A. 2008, ApJ, 688, 1159
Nakamura, K., Takiwaki, T., Kuroda, T., & Kotake, K. 2014, arXiv:1406.2415
Nomoto, K., & Hashimoto, M. 1988, Phys. Rep., 163, 13
Nordhaus, J., Burrows, A., Almgren, A., & Bell, J. 2010, ApJ, 720, 694
O'Connor, E., & Ott, C. D. 2011, ApJ, 730, 70
—. 2013, ApJ, 762, 126
Ohnishi, N., Kotake, K., & Yamada, S. 2006, ApJ, 641, 1018
Pejcha, O., & Thompson, T. A. 2012, ApJ, 746, 106
Rampp, M., & Janka, H. 2000, ApJ, 539, L33
Stone, J. M., & Norman, M. L. 1992, ApJS, 80, 753
Sukhbold, T., & Woosley, S. E. 2014, ApJ, 783, 10
Sumiyoshi, K., Yamada, S., Suzuki, H., Shen, H., Chiba, S., & Toki, H. 2005, ApJ, 629, 922
Suwa, Y. 2014, PASJ, 66, L1
Suwa, Y., Kotake, K., Takiwaki, T., Liebendörfer, M., & Sato, K. 2011, ApJ, 738, 165
Suwa, Y., Kotake, K., Takiwaki, T., Whitehouse, S. C., Liebendörfer, M., & Sato, K. 2010, PASJ, 62, L49
Suwa, Y., Takiwaki, T., Kotake, K., Fischer, T., Liebendörfer, M., & Sato, K. 2013, ApJ, 764, 99
Takiwaki, T., Kotake, K., & Suwa, Y. 2012, ApJ, 749, 98
—. 2014, ApJ, 786, 83
Thompson, T. A., Burrows, A., & Pinto, P. A. 2003, ApJ, 592, 434
Ugliano, M., Janka, H.-T., Marek, A., & Arcones, A. 2012, ApJ, 757, 69
Woosley, S. E., & Heger, A. 2007, Phys. Rep., 442, 269
Woosley, S. E., Heger, A., & Weaver, T. A. 2002, Reviews of Modern Physics, 74, 1015
Woosley, S. E., & Weaver, T. A. 1995, ApJS, 101, 181